J Neurooncol (2011) 103:619–627
DOI 10.1007/s11060-010-0433-0

CLINICAL STUDY – PATIENT STUDY

Prediction of malignancy grading using computed tomography perfusion imaging in nonenhancing supratentorial gliomas

Takaaki Beppu · Makoto Sasaki · Kohsuke Kudo · Akira Kurose · Masaru Takeda · Hiroshi Kashimura · Akira Ogawa · Kuniaki Ogasawara

Received: 10 June 2010 / Accepted: 20 September 2010 / Published online: 15 October 2010

Abstract Tumor grade differentiation is often difficult using routine neuroimaging alone. Computed tomography perfusion imaging (CTP) provides quantitative information on tumor vasculature that closely parallels the degree of tumor malignancy. This study examined whether CTP is useful for preoperatively predicting the grade of malignancy in glioma showing no enhancement on contrast-enhanced magnetic resonance imaging (MRI). Subjects comprised 17 patients with supratentorial glioma without enhancement on MRI. CTP was performed preoperatively, and absolute values and normalized ratios of parameters were calculated. Postoperatively, subjects were classified into two groups according to histological diagnosis of grade 3 (G3) glioma or grade 2 (G2) glioma. Absolute values and normalized ratios for each parameter were compared between G3 and G2. Accuracies of normalized ratios for cerebral blood flow (*n*CBF) and cerebral blood volume (*n*CBV) in predicting a diagnosis of G3 were assessed. In addition, *n*CBV was compared between diffuse astrocytoma, G2 oligodendroglial tumor (OT), and G3 OT. Values for *n*CBF and *n*CBV differed significantly between G3 and G2. Using *n*CBV of 1.6 as a cutoff, specificity and sensitivity for distinguishing G3 were 83.3% and 90.9%, respectively. No significant difference in *n*CBV was seen between diffuse astrocytoma and G2 OT, whereas differences were noted between G2 and G3 OTs, and between diffuse astrocytoma and G3 OT. CTP offers a useful method for differentiating between G3 and G2 in nonenhancing gliomas.

Keywords Computed tomography perfusion imaging · Diffuse astrocytoma · Glioma · Nonenhancement · Oligodendroglioma · Preoperative diagnosis

T. Beppu (✉) · M. Takeda · H. Kashimura · A. Ogawa · K. Ogasawara
Department of Neurosurgery, Iwate Medical University, Uchimaru 19-1, Morioka 020-8505, Japan
e-mail: tbeppu@iwate-med.ac.jp

M. Sasaki · K. Kudo
Advanced Medical Research Center, Iwate Medical University, Morioka, Japan

A. Kurose
Department of Pathology, Iwate Medical University, Morioka, Japan

Introduction

Glioma is graded according to World Health Organization (WHO) classification, with grade 1 or 2 graded as low-grade glioma (LGG) and grade 3 or 4 commonly defined as high-grade glioma (HGG) [1]. As treatment and prognosis differ substantially between LGG and HGG, the ability to differentiate between grade 2 (G2) glioma and grade 3 (G3) glioma, as the border between LGG and HGG, is very important. On contrast-enhanced computed tomography (CT) and magnetic resonance imaging (MRI), G2 gliomas are nonenhanced due to preservation of blood–brain barrier (BBB), whereas G3 gliomas are commonly enhanced due to increased vascular permeability caused by disruption of the BBB within the tumor [2–4]. However, the relationship between histological grading and contrast enhancement on CT and MRI is not always clear. Preoperatively differentiating between G3 and G2 gliomas that are nonenhanced on conventional neuroimaging is often difficult. When patients with nonenhancing glioma are encountered, neurooncologists may perform various examinations to differentiate between G3 and G2 gliomas, such as positron emission tomography (PET) for direct assessment of tumor

metabolism, magnetic resonance spectroscopy to detect magnetic resonance signals of metabolites, and diffusion-weighted MRI to clarify structures within and surrounding the tumor. Assessment of intratumoral vasculature is one approach that may help to clarify the intratumoral biological characteristics and malignancy of a tumor, as intratumoral angiogenesis and high vascularity, which are regulated by hypoxia and various vascular endothelial growth factors, are essential for tumor growth and progression [5–7].

Angiography enables direct observation of intratumoral vessels, but is hazardous and remains limited for depiction of intratumoral microvasculature. Magnetic resonance perfusion imaging (MRP) and CT perfusion imaging (CTP) provide reliable information on the intratumoral microvasculature [8–12]. Numerous studies of perfusion imaging have shown that increasing malignancy of the glioma is associated with increased intratumoral blood volume and vascular permeability [10, 13–15]. Quantitative evaluation from perfusion imaging thus depends on both the microvasculature (vascular density and diameter), and vascular permeability due to disruption or absence of the BBB within the tumor. Previous reports have shown good correlations between findings on perfusion imaging and malignancy grading in enhancing glioma. In contrast, the BBB of vessels is preserved in nonenhancing glioma, since extravasation of contrast medium through the BBB in tumor vessels is considered to represent the main cause of tumor contrast enhancement [4]. As MRI remains the preferred technique for assessing brain tumors, studies using MRP to thoroughly evaluate gliomas greatly outnumber those using CTP, and MRP has also been applied to neurooncological applications for nonenhancing gliomas, such as determining biopsy targets and predicting malignant progression [16–18]. In recent years, CTP has gained acceptance as a valuable imaging technique for assessing hemodynamics in brain tumors [13, 14, 19–22]. However, whether CTP is useful for grading malignancy of nonenhancing gliomas remains unclear. CTP retains the advantage of a linear relationship between attenuation changes on CT and tissue concentration of contrast medium, unlike MRP [8, 20]. We therefore hypothesized that CTP should accurately provide quantitative information on only the microvasculature within the tumor, excluding extravasation due to permeability, when limited to patients with nonenhancing glioma. In the present study, we performed CTP on patients with nonenhancing glioma, and compared cerebral blood volume (CBV), cerebral blood flow (CBF), and mean transit time (MTT), as quantitative values provided from CTP, with postoperative histological diagnosis. The present study aims to determine whether CTP is useful for prediction of preoperative malignancy grading (WHO G2 or G3) in nonenhancing glioma on contrast-enhanced MRI.

Patients and methods

Patients

The study protocol was approved by the Ethics Committee of Iwate Medical University, Morioka, Japan. Consecutive patients admitted to the Department of Neurosurgery at Iwate Medical University between September 2006 and January 2010 and meeting the entry criteria were recruited to this study. Entry criteria for this study comprised: diagnosis of supratentorial glioma; tumor bulk not clearly enhanced on gadolinium-enhanced T1-weighted MRI (Gd-T1WI); tumor bulk sited in the supratentorial cerebrum; no past history relating to the brain, including surgical operation, irradiation, administration of anticancer agents or steroids, stroke, infection, or other disorders such as demyelinating disease; and provision of written informed consent to participate. Subjects comprised 17 patients (7 men, 10 women) with mean age of 47.8 years. Patient data including age, tumor site, operation method, postoperative histological diagnosis, and malignancy grade are summarized in Table 1.

Table 1 Patient summary

No.	Age (years)	Tumor site	Surgery	Histology	WHO grade
1	76	Temporal lobe	Biopsy	AA	3
2	58	Frontal lobe	Resection	AO	3
3	45	Frontal lobe	Resection	AO	3
4	34	Frontal lobe	Resection	AO	3
5	29	Frontal lobe	Resection	AO	3
6	21	Frontal lobe	Resection	AOA	3
7	78	Frontal lobe	Biopsy	DA	2
8	68	Frontal lobe	Biopsy	DA	2
9	68	Parietal lobe	Biopsy	DA	2
10	65	Frontal lobe	Resection	DA	2
11	58	Frontal lobe	Resection	DA	2
12	52	Frontal lobe	Resection	Oli	2
13	46	Temporal lobe	Resection	Oli	2
14	42	Frontal lobe	Resection	OA	2
15	30	Frontal lobe	Resection	OA	2
16	27	Frontal lobe	Resection	DA	2
17	16	Temporal lobe	Resection	OA	2

AA anaplastic astrocytoma, *AO* anaplastic oligodendroglioma, *AOA* anaplastic oligoastrocytoma, *DA* diffuse astrocytoma, *Oli* oligodendroglioma, *OA* oligoastrocytoma

Conventional MRI and CTP

Conventional MRI was performed for all subjects within 7 days before surgery. Spin-echo Gd-T1WI was performed approximately 2 min after intravenous injection of gadolinium (0.2 ml/kg, Magnevist; Bayer Schering Pharma, Berlin, Germany), using a 3.0-T whole-body scanner (GE Yokogawa Medical Systems, Tokyo, Japan) with a standard head coil. We confirmed that the tumor in each patient did not show clear enhancement with gadolinium on Gd-T1WI.

CTP was also performed within 7 days before surgery using a 16-row multidetector CT system (Aquillion 16; Toshiba Medical Systems, Tokyo, Japan), in accordance with the methods described by Sasaki et al. [23]. After performing noncontrast CT to determine the location of the tumor balk, a multislice scan targeting the tumor bulk was performed (80 kV_p; 40 mA; 1.5 s/rotation, 30 rotations field of view, 240 × 240 mm^2; four contiguous 8-mm-thick sections; total scan time, 45 s). Five seconds after intravenously injecting 40 ml (4 ml/s) nonionic iodine contrast medium (Iopamiron 300; Bayer Schering Pharma) using a power injector, dynamic scanning was started and tissue attenuation of contrast medium was monitored on a slice. Radiation doses for the scanning protocol were as follows: volume CT dose index, 150 mGy; dose–length product, 480 mGy cm; and effective dose, 1.34 mSv. Data were transferred to a commercial workstation (M900 Quadra; Ziosoft, Tokyo, Japan), and scaled color maps for CBF, CBV, and MTT were automatically created. All mathematical analyses were performed by the deconvolution method [19, 24], using CTP analysis software supplied with the workstation described above. Among the three types of deconvolution algorithms implemented in this software, we used the block-circulant singular value decomposition method. Regions of interest (ROI) for venous output and arterial input functions were manually placed at the superior sagittal sinus and a single branch of the insular segment of the middle cerebral artery on either the pathological or nonpathological side, or A2 segment of the anterior cerebral artery, respectively. ROI were also placed over the entire tumor bulk and apparently normal white matter (ANWM) on the nonpathological side, on color maps for each parameter. Size of the ROI for ANWM was established as 1.0 cm^2. In the measurement of absolute values, the vascular-pixel elimination (VPE) method was used to exclude pixels from large vessels at the cerebral surface, sulci, and cisterns [23, 25]. In the present study, we established the VPE threshold as 6.0 ml/100 g for CBV, since high-CBV areas suggesting large cortical vessels on color map disappeared satisfactorily at 6.0 ml/100 g when the threshold was varied between 5.0 and 8.0 ml/100 g using our analysis software. Large vascular pixels were thus defined as pixels with CBV values >6.0 ml/100 g and were automatically eliminated. Regional absolute values (*r*CBF, *r*CBV, and *r*MTT) were then calculated automatically for all ROI. The measurements described above were performed twice for each patient by two investigators (M.S. and K.K.) who were blinded to all clinical data, including individual patient information and histological diagnosis. Absolute values of all parameters for each patient were determined as the mean of four measured values, as determined twice by each investigator. The second test was performed 1 week after the first test, with a different randomized order of measurements from the first test. We also calculated normalized ratios (*n*CBF, *n*CBV, and *n*MTT) as the absolute value for the tumor divided by the absolute value for the ANWM for each parameter in all patients. All patients underwent surgery, with tumor resection for 13 patients and CT-guided stereotactic needle biopsy for 4 patients (Table 1). The region targeted in stereotactic biopsy was based on findings from the CBV color map. If the color map showed heterogeneous perfusion within the tumor, the targeted region corresponded to the region with the highest perfusion area for CBV. In cases with tumor resection, histological diagnosis was determined by observation at the lesion showing the most malignant histological features in all preparations. Postoperatively, histological diagnosis using specimens obtained from surgery was made by one of the investigators (A.K.) with no prior knowledge of CTP data.

Statistical analyses

All data were analyzed using PASW Statistics version 18 software (SPSS Japan, Tokyo, Japan). Inter- and intrarater reliabilities for all absolute values were evaluated according to classification of the intraclass correlation coefficient (ICC) [26]. For $ICC_{(1,1)}$ and $ICC_{(1,k)}$ as interrater reliability, agreement of all absolute values (CBF, CBV, and MTT) between first and second tests was analyzed for tumor and ANWM for each investigator, using one-factor analysis of variance (ANOVA). For $ICC_{(2,1)}$ and $ICC_{(2,k)}$ as intrarater reliability, agreement of all absolute values between the two investigators was analyzed for tumor and ANWM for each test, using two-factor ANOVA. Patients were assigned to one of two histological grading groups according to histological classification: WHO G2 or WHO G3. Frequency of biopsy was compared between G2 and G3 groups using Fisher's exact probability test. We compared absolute values from the tumor lesion for each parameter between G2 and G3 using the Mann–Whitney *U* test. Furthermore, the normalized ratio for each parameter was compared between these groups again using the Mann–Whitney *U* test. The accuracy of *r*CBF and *n*CBV in predicting a diagnosis of G3 was assessed using receiver

operating characteristic (ROC) curves. ROC curves were calculated in increments of 0.1. Absolute values and normalized ratios for CBV were compared between diffuse astrocytoma, G2 oligodendroglial tumor (OT), and G3 OT, using the Mann–Whitney U test. G2 OTs comprised oligodendroglioma or oligoastrocytoma, whereas G3 OTs comprised anaplastic oligodendroglioma or anaplastic oligoastrocytoma. Statistical significance was established at the $P < 0.05$ level in all analyses.

Results

Based on histological diagnosis after surgery, 6 patients were assigned to the G3 group and 11 patients were assigned to the G2 group (Table 1). Of these 17 patients, 4 patients underwent stereotactic biopsy. Frequency of biopsy did not differ significantly between G3 and G2 groups ($P = 0.25$).

Interrater reliability was classified as "almost perfect" for both tumor and ANWM for each investigator: $ICC_{(1,1)}$ and $ICC_{(1,k)}$ for M.S. were 0.943 and 0.971 for tumor, and 0.961 and 0.980 for ANWM, respectively, and those for K.K. were 0.966 and 0.983 for tumor, and 0.942 and 0.970 for ANWM, respectively. Intrarater reliability was also classified as "almost perfect" for both tumor and ANWM in each test: $ICC_{(2,1)}$ and $ICC_{(2,k)}$ in the first test were 0.987 and 0.993 for tumor, and 0.973 and 0.987 for ANWM, respectively, and those in the second test were 0.971 and 0.985 for tumor, and 0.973 and 0.986 for ANWM, respectively. Absolute values of tumor lesions for each parameter in G3 and G2 groups are summarized in Table 2. Absolute values for all parameters varied widely, with no significant differences in any parameters identified between G3 and G2 groups. Normalized ratios for each parameter are summarized in Table 3. Significant differences between G3 and G2 groups were identified for nCBF and nCBV, with no significant differences in nMTT.

The cutoff for accuracy was defined as the point lying closest to the upper-left corner of the ROC curve.

Table 2 Absolute values for each parameter

	rCBF (ml/100 g/min)	rCBV (ml/100 g)	rMTT (s)
G3 ($n = 6$)			
Range	10.8–27.0	1.9–3.2	6.8–10.8
Mean ± SD	18.3 ± 5.3	2.5 ± 0.5	8.5 ± 1.5
G2 ($n = 11$)			
Range	8.8–23.3	1.3–2.6	7.0–12.2
Mean ± SD	15.5 ± 4.2	2.1 ± 0.4	8.8 ± 1.5
P	0.27	0.25	0.76

SD standard deviation

Table 3 Normalized ratios for each parameter

	nCBF	nCBV	nMTT
G3 ($n = 6$)			
Range	1.34–3.00	1.54–2.39	0.76–1.06
Mean ± SD	2.10 ± 0.57	1.92 ± 0.37	0.90 ± 0.12
G2 ($n = 11$)			
Range	0.92–2.00	0.91–1.75	0.79–1.07
Mean ± SD	1.41 ± 0.38	1.26 ± 0.28	0.91 ± 0.09
P	0.01	0.004	0.76

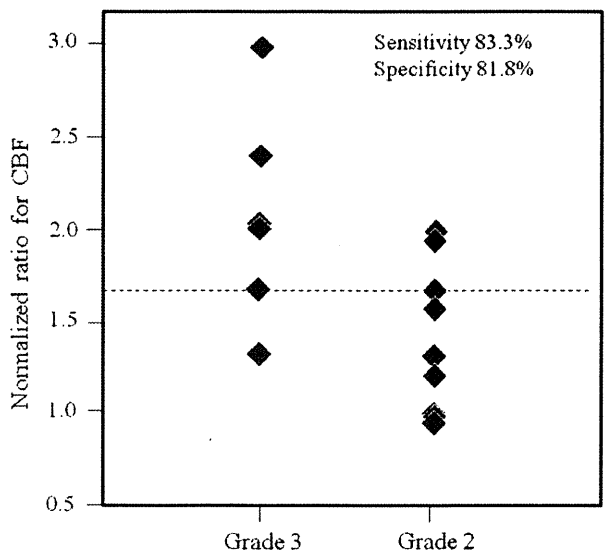

Fig. 1 Relationship between nCBF value and WHO grading. Using a cutoff of 1.7 (*dashed line*), nCBV was ≥1.7 for 5 (83.3%) of 6 patients with G3, compared with <1.7 for 9 (63.6%) of 11 patients with G2

Sensitivity and specificity in predicting a diagnosis of G3 were 83.3% and 81.8% for nCBF (cutoff 1.7), and 83.3% and 90.9% for nCBV (cutoff 1.6) (Figs. 1, 2). Accuracy for predicting a diagnosis of G3 was higher with nCBV than with nCBF.

A comparison of nCBV was made between G3 OT, G2 OT, and diffuse astrocytoma (Table 4). Significant differences in nCBV were identified between G3 and G2 OTs ($P = 0.009$), and between G3 OT and diffuse astrocytoma ($P = 0.02$), whereas no significant difference was seen between G2 OT and diffuse astrocytoma ($P = 0.36$).

Illustrative cases

We now describe the cases of two patients for whom CTP provided useful information for predicting tumor grading. Gd-T1WI for case 6 showed glioma with no clear enhancement in the right frontal lobe (Fig. 3a). Using the

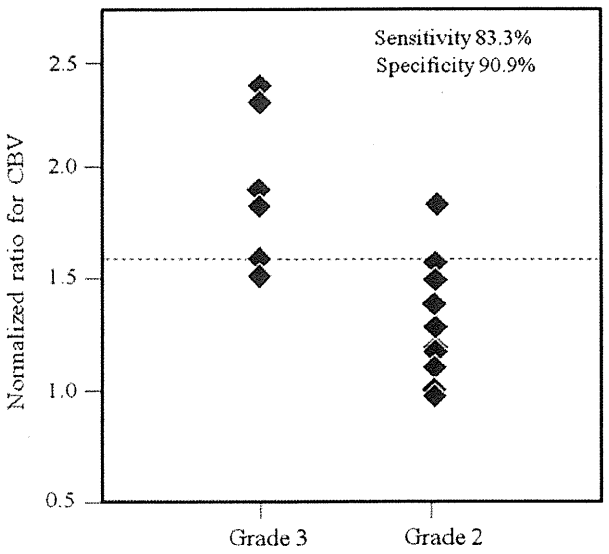

Fig. 2 Relationship between *n*CBV value and WHO grading. Using a cutoff point of 1.6 (*dashed line*), *n*CBV was ≥1.6 for 5 (83.3%) of 6 patients with G3 and <1.6 for 10 (90.9%) of 11 patients with G2

Table 4 Normalized ratio (mean ± SD) for CBV in G3 OT, G2 OT, and diffuse astrocytoma

	*n*CBV
G3 OT ($n = 5$)	1.99 ± 0.36
G2 OT ($n = 5$)	1.16 ± 0.24
Diffuse astrocytoma ($n = 6$)	1.35 ± 0.31

OT oligodendroglial tumors

VPE method, color mapping of CBV demonstrated large vessels of the cerebral surface to be successfully excluded (Fig. 3b). Color mapping of CBV depicted areas of hyperperfusion within the tumor. The *n*CBV for this case (*n*CBV = 2.3) was higher than the cutoff point. Tissue specimens obtained from gross total resection showed typical histological features of G3 anaplastic oligoastrocytoma.

Gd-T1WI for case 14 showed nonenhancing glioma of the right frontal lobe (Fig. 4a). The VPE method satisfactorily eliminated large vessels of the cerebral surface (Fig. 4b). On color mapping, areas of hyperperfusion seemed to be minor compared with those in case 6. The *n*CBV in this case (*n*CBV = 1.2) was lower than the cutoff point. After tumor resection, histological diagnosis was G2 oligoastrocytoma.

Discussion

Previous reports have documented that G3 gliomas make up 40–46% of nonenhancing gliomas on conventional MRI [3, 4]. Our finding of G3 tumors in 6 (35.2%) of 17 patients

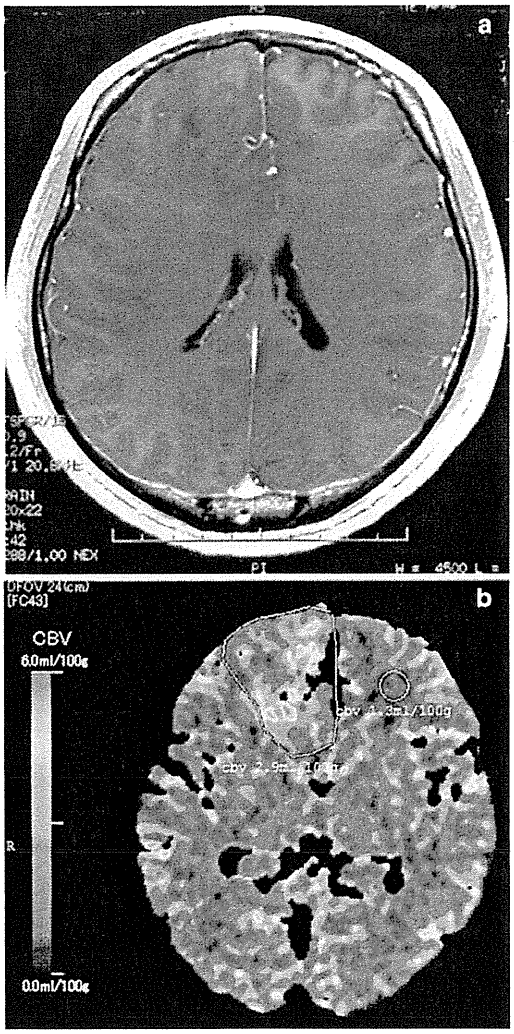

Fig. 3 Gd-T1WI (**a**) and color map of CBV (**b**) for case 6. *Circle* ROI covering the entire tumor bulk and ANWM localized on the nonpathological side

was close to this level. Thus, preoperative differentiation between G3 and G2 using MRI is often difficult. Biopsy or resection allowing histological diagnosis currently remain the basis for differentiation between G3 and G2 gliomas. However, neuroimaging can provide useful information on pathological diagnosis, particularly for patients who do not undergo biopsy or resection allowing histological diagnosis. Novel neuroimaging procedures other than routine MRI are thus desired. CTP and MRP provide reliable information on tumor vasculature, which can help to determine the extent of malignancy in glioma [8, 10, 22]. Although limitations of CTP include radiation dose and limited area of coverage compared with MRP, the linear relationship between attenuation changes on CT and tissue concentration of contrast medium and the lack of confounding sensitivity to flow artifacts allow CTP to

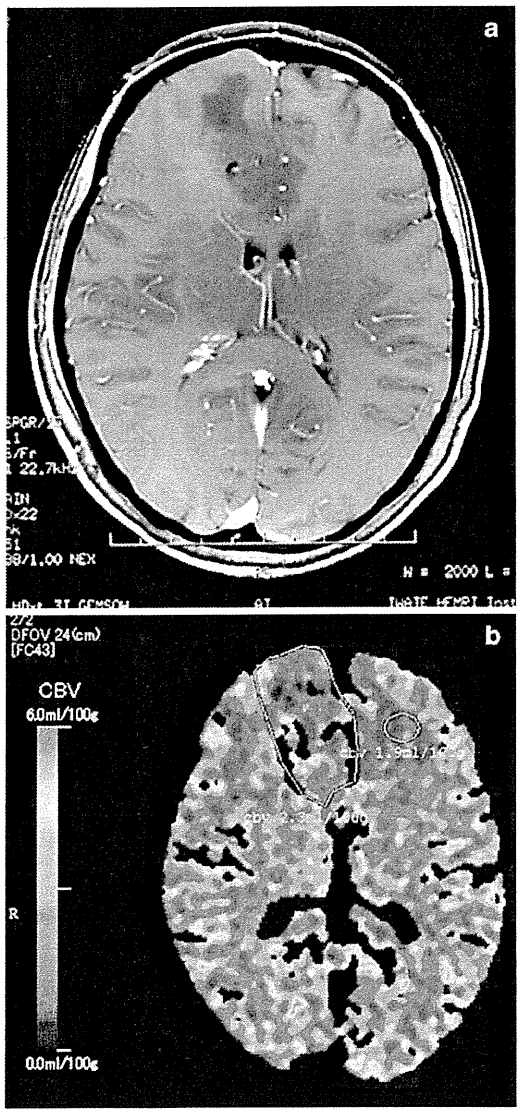

Fig. 4 Gd-T1WI (**a**) and color map of CBV (**b**) for case 14. *Circle* ROI covering the entire tumor bulk and ANWM localized on the nonpathological side

potentially offer a more accurate representation of tissue microvasculature than similar MRP studies [8, 20]. Furthermore, CTP offers advantages such as measurement of quantitative absolute values, greater availability, fast scanning time, high spatial resolution, low cost, and the ability to use this technique for patients who cannot undergo MRI due to the presence of metallic materials in the body [14, 22, 27].

CBF derived from CTP has been suggested to show a tendency toward overestimation, compared with that derived from PET [28]. Since overestimation of CBF in CTP was attributable to the presence of large vessels on the cerebral surface, as contrast materials act as a nondiffusible intravascular tracer in CTP unlike in PET, the VPE method has been proposed to eliminate flow in large vessels [25]. Accurate measurement of CBV contributes to accurate CBF and MTT, as these parameters are closely associated in the central volume principle as CBF = CBV/MTT [29]. We therefore used the VPE method in the present study. We think that optimal threshold differs according to the specific analysis software used for CTP. While VPE threshold was 8.0 ml/100 g in the report by Kudo et al. [25], we established a threshold of 6.0 ml/100 g, since high-CBV areas from cortical large vessels disappeared satisfactorily at this threshold for the analysis software used in our study. Another reason for using the VPE method is that OTs are commonly seen as superficially located tumors in the brain [30, 31]. Elimination of superficial large vessels at the cerebral surface, sulci, and cisterns thus seems warranted when CTP is performed for OTs.

In previous reports of CTP, *r*CBV values ranged from 2.3 to 8.87 ml/100 g for HGG and from 0.95 to 3.28 ml/100 g for LGG, differing significantly between HGG and LGG [13, 14, 20]. The present mean rCBV values in G3 and G2 (Table 2) agreed with previous findings. In addition, mean rCBV values in both G3 and G2 were less than half of 6.0 ml/100 g as VPE threshold. These findings suggest that the VPE method used in this study did not exclude tumor vessels along with other large vessels from CBV maps. While *r*CBV for G3 tended to be on the low side compared with previous reports, this could have resulted from the exclusion of patients with enhancing glioma as subjects in this study. Extravasation of contrast medium through the BBB in enhanced glioma may directly lead to increased CBV, due to the linear relationship between attenuation changes on CT and tissue concentration of contrast medium. Jain et al. [20] documented that *r*CBF and *r*CBV in nonenhancing G3 glioma do not differ significantly from those in nonenhancing G2 glioma, although sample size in that report was small. The present study with more subjects suggested that even nonenhancing G3 glioma retains more vascular density than G2, although the difference in *r*CBV between the two groups was minor (Table 2). However, this result might have been influenced by the disproportionate number of OTs in the G2 (42%) and G3 (83%) groups. If vascular density is significantly higher in G3 OT than in anaplastic astrocytoma, the large number of G3 OTs may have result in a high mean CBV for the G3 group in this study. This issue represents a definite limitation to the present study.

Concentration of contrast medium within the tumor might be subtly influenced by individual parameters such as body size and cardiac output volume, and differences in analytical software among institutes. We must emphasize the importance of estimation using normalized ratios, as

this allows us to ignore these differences. Ellika et al. [22] reported findings for *n*CBV using CTP in 19 patients with glioma, composed of a mixture of enhancing and nonenhancing WHO G1–G4 gliomas, and the utility of *n*CBF and *n*CBV for distinguishing HGG from LGG. They also documented *n*CBF and *n*CBV ranges of 0.78–3.75 and 1.5–3.7 in two patients with nonenhancing G3 glioma, and ranges of 1.26–1.48 and 0.94–1.72 in three patients with nonenhancing G2 glioma, respectively. Mean values of *n*CBF and *n*CBV in G3 and G2 in this study (Table 3) seemed close to the values reported by Ellika et al.

Radiographic grading of gliomas with conventional MRI is not always accurate, with 85.7% sensitivity for predicting HGG, even when including subjects with enhancing glioma [22]. When subjects are limited to those with nonenhancing gliomas, radiographic grading using conventional MRI should be more difficult. A previous report documented 85.7% sensitivity and 100% specificity for identifying HGG using *n*CBV [22]. In the present study, CTP could distinguish nonenhancing G3 glioma from nonenhancing G2 glioma with 83.3% sensitivity and 90.9% specificity using *n*CBV (Fig. 2). This was superior to the results for *n*CBF. Accuracy for distinguishing G3 using *n*CBV in the present study was by no means inferior to that reported by Ellika et al. [22], but subjects in this study were limited to those with nonenhancing glioma. These results suggest that *n*CBV in CTP is useful as an auxiliary examination in addition to routine neuroimaging for predicting the grade of malignancy in nonenhancing gliomas.

Previous studies using MRP have documented higher relative CBV in OT than in other gliomas [32–34]. Lev et al. [33] suggested that OTs tend to appear as high blood volume lesion on MRP, without respect to tumor grade. Two reports using MRP documented that G2 OTs show higher relative CBV than diffuse astrocytoma [32, 34]. Also in a report using CTP by Narang et al. [15], G2 OTs showed a trend towards higher CBV than G2 astrocytic tumors, although no significant difference was found, and no significant difference in CBV between G3 OTs and G2 OTs was identified. Those reports explained the high relative CBV of OT by a hypothesis based on the specific histological features of fine capillary networks [33]. Furthermore, those reports suggested that grading malignancy may be difficult when patients with OT are included, due to a high relative CBV. In the present study, no significant difference in *n*CBV was seen between diffuse astrocytoma and G2 OT, whereas significant differences were found between G3 OT and G2 OT. The difference between the reports described above and the present investigation might be explained by differences between MRP and CTP, and by the use of the VPE method in this study. Signal changes in dynamic susceptibility contrast (DSC) MRI for MRP do not depend on only the concentration of contrast material, but also on T2* or T2 relaxation rates, which are affected by calcified foci and hemorrhage within tumor tissue. These histological features are commonly seen in OTs. DSC signals might thus be higher in OTs than in diffuse astrocytoma, even when the microvascular densities are comparable. The VPE method may have eliminated pixels of high-CBV vessels in OTs, if vascular density in OTs is significantly higher than that in diffuse astrocytoma. However, exclusion of large vessels at the cerebral surface and sulci from CTP maps is important, as OTs grow superficially in the brain. Cha et al. [32] explained for reason of high relative CBV for OTs in MRP by the predominant cortical location in addition to distinct vascular pattern in OTs. We think that CTP with the VPE method is useful for simple malignancy grading in subjects with OTs. Conversely, MRP offers potential advantages for the diagnosis of OTs. However, CTP should not be performed additionally to MRP if the purpose in examination is achieved by MRP, as CTP retains drawbacks such as radiation dose and iodine contrast medium.

The present study possesses some limitations regarding the interpretation of study results. First, the number of patients in this study was small, with remarkably fewer cases of anaplastic astrocytoma compared with OT in G3, as mentioned above. Further investigation including a larger number of cases of anaplastic astrocytoma is needed. A second limitation is the possible discrepancy between histological diagnosis and the region of highest CBV within the tumor. The region targeted for stereotactic biopsy was not rigorously transferred from the region of highest *r*CBV ("hot spots"). However, risk of histological misdiagnosis caused by sampling error during biopsy might be negligible, since the number of patients who underwent biopsy was small in both G3 and G2, and no significant difference in frequency of biopsy was seen between groups. In patients who underwent tumor resection, histological diagnosis was not made using tissue specimens rigorously corresponding to "hot spots." However, histological diagnosis based on the most malignant histological features should be closely associated with high CBV, as increased malignancy is associated with higher vascular density. CTP with a 16-row multidetector CT scanner, covering only four contiguous 8-mm-thick sections, did not cover the entire tumor bulk in some patients. For those patients, histological diagnosis was made using tumor tissues corresponding to the area depicted in CTP. A third limitation was that data calculated from CTP in this study were not the highest CBV values for a small ROI placed in "hot spots" on a color map, but rather were mean values for a large ROI covering the entire tumor bulk. This issue also influences the second limitation. We thought that the simple protocol in this study, combining absolute values as a mean in a large ROI with histological diagnosis from the

area of the most malignant features, is suitable for application in clinical practice, as tissue sampling error of regions corresponding to a small ROI can be avoided. High ICC in inter- and intrarater reliabilities showed that the protocol used in this study offers high reproducibility.

Conclusions

We performed CTP combined with the VPE method for 17 patients, to clarify whether CTP can accurately differentiate between G3 and G2 nonenhancing glioma. Our results showed that *n*CBV from CTP was highly accurate in differentiating G3 from G2 nonenhancing gliomas. The most important result was that CTP enabled differentiation between G3 and G2 nonenhancing OTs. CTP combined with the VPE method offers a useful technique for differentiating between G3 and G2 in nonenhancing gliomas.

Acknowledgments This study was supported in part by a Grant-in-Aid for Advanced Medical Science Research from the Ministry of Science, Education, Sports, and Culture, Japan.

References

1. Louis DN, Ohgaki H, Wiestler OD, Cavenee WK, Burger PC, Jouvet A, Scheithauer BW, Kleihues P (2007) The 2007 WHO classification of tumours of the central nervous system. Acta Neuropathol 114:97–109
2. Dean BL, Drayer BP, Bird CR, Flom RA, Hodak JA, Coons SW, Carey RG (1990) Gliomas: classification with MR imaging. Radiology 174:411–415
3. Ginsberg LE, Fuller GN, Hashmi M, Leeds NE, Schomer DF (1998) The significance of lack of MR contrast enhancement of supratentorial brain tumors in adults: histopathological evaluation of a series. Surg Neurol 49:436–440
4. Mihara F, Numaguchi Y, Rothman M, Kristt D, Fiandaca M, Swallow L (1995) Non-enhancing supratentorial malignant astrocytomas: MR features and possible mechanisms. Radiat Med 13:11–17
5. Jain RK, Gerlowski LE (1986) Extravascular transport in normal and tumor tissues. Crit Rev Oncol Hematol 5:115–170
6. Shweiki D, Itin A, Soffer D, Keshet E (1992) Vascular endothelial growth factor induced by hypoxia may mediate hypoxia-initiated angiogenesis. Nature 359:843–845
7. Vajkoczy P, Menger MD (2000) Vascular microenvironment in gliomas. J Neurooncol 50:99–108
8. Barnett G (2006) High-grade gliomas. Humana, Totowa
9. Law M, Cha S, Knopp EA, Johnson G, Arnett J, Litt AW (2002) High-grade gliomas and solitary metastases: differentiation by using perfusion and proton spectroscopic MR imaging. Radiology 222:715–721
10. Law M, Yang S, Wang H, Babb JS, Johnson G, Cha S, Knopp EA, Zagzag D (2003) Glioma grading: sensitivity, specificity, and predictive values of perfusion MR imaging and proton MR spectroscopic imaging compared with conventional MR imaging. Am J Neuroradiol 24:1989–1998
11. Eastwood JD, Lev MH, Provenzale JM (2003) Perfusion CT with iodinated contrast material. Am J Roentgenol 180:3–12
12. Hoeffner EG, Case I, Jain R, Gujar SK, Shah GV, Deveikis JP, Carlos RC, Thompson BG, Harrigan MR, Mukherji SK (2004) Cerebral perfusion CT: technique and clinical applications. Radiology 231:632–644
13. Ding B, Ling HW, Chen KM, Jiang H, Zhu YB (2006) Comparison of cerebral blood volume and permeability in preoperative grading of intracranial glioma using CT perfusion imaging. Neuroradiology 48:773–781
14. Eastwood JD, Provenzale JM (2003) Cerebral blood flow, blood volume, and vascular permeability of cerebral glioma assessed with dynamic CT perfusion imaging. Neuroradiology 45:373–376
15. Narang J, Jain R, Scarpace L, Saksena S, Schultz LR, Rock JP, Rosenblum M, Patel SC, Mikkelsen T (2010) Tumor vascular leakiness and blood volume estimates in oligodendrogliomas using perfusion CT: an analysis of perfusion parameters helping further characterize genetic subtypes as well as differentiate from astroglial tumors. J Neurooncol. doi:10.1007/s11060-010-0317-3
16. Maia AC Jr, Malheiros SM, da Rocha AJ, Stavale JN, Guimaraes IF, Borges LR, Santos AJ, da Silva CJ, de Melo JG, Lanzoni OP, Gabbai AA, Ferraz FA (2004) Stereotactic biopsy guidance in adults with supratentorial nonenhancing gliomas: role of perfusion-weighted magnetic resonance imaging. J Neurosurg 101:970–976
17. Danchaivijitr N, Waldman AD, Tozer DJ, Benton CE, Brasil Caseiras G, Tofts PS, Rees JH, Jager HR (2008) Low-grade gliomas: do changes in rCBV measurements at longitudinal perfusion-weighted MR imaging predict malignant transformation? Radiology 247:170–178
18. Price SJ (2010) Advances in imaging low-grade gliomas. Adv Tech Stand Neurosurg 35:1–34
19. Nabavi DG, Cenic A, Craen RA, Gelb AW, Bennett JD, Kozak R, Lee TY (1999) CT assessment of cerebral perfusion: experimental validation and initial clinical experience. Radiology 213: 141–149
20. Jain R, Ellika SK, Scarpace L, Schultz LR, Rock JP, Gutierrez J, Patel SC, Ewing J, Mikkelsen T (2008) Quantitative estimation of permeability surface-area product in astroglial brain tumors using perfusion CT and correlation with histopathologic grade. Am J Neuroradiol 29:694–700
21. Jain R, Scarpace L, Ellika S, Schultz LR, Rock JP, Rosenblum ML, Patel SC, Lee TY, Mikkelsen T (2007) First-pass perfusion computed tomography: initial experience in differentiating recurrent brain tumors from radiation effects and radiation necrosis. Neurosurgery 61:778–786
22. Ellika SK, Jain R, Patel SC, Scarpace L, Schultz LR, Rock JP, Mikkelsen T (2007) Role of perfusion CT in glioma grading and comparison with conventional MR imaging features. Am J Neuroradiol 28:1981–1987
23. Sasaki M, Kudo K, Ogasawara K, Fujiwara S (2009) Tracer delay-insensitive algorithm can improve reliability of CT perfusion imaging for cerebrovascular steno-occlusive disease: comparison with quantitative single-photon emission CT. Am J Neuroradiol 30:188–193
24. Wintermark M, Maeder P, Thiran JP, Schnyder P, Meuli R (2001) Quantitative assessment of regional cerebral blood flows by perfusion CT studies at low injection rates: a critical review of the underlying theoretical models. Eur Radiol 11:1220–1230
25. Kudo K, Terae S, Katoh C, Oka M, Shiga T, Tamaki N, Miyasaka K (2003) Quantitative cerebral blood flow measurement with dynamic perfusion CT using the vascular-pixel elimination method: comparison with H2(15)O positron emission tomography. Am J Neuroradiol 24:419–426
26. Shrout PE, Fleiss JL (1979) Intraclass correlations: uses in assessing rater reliability. Psychol Bull 86:420–428
27. Miles KA, Charnsangavej C, Lee FT, Fishman EK, Horton K, Lee TY (2000) Application of CT in the investigation of angiogenesis in oncology. Acad Radiol 7:840–850

28. Gillard JH, Minhas PS, Hayball MP, Bearcroft PW, Antoun NM, Freer CE, Mathews JC, Miles KA, Pickard JD (2000) Assessment of quantitative computed tomographic cerebral perfusion imaging with H2(15)O positron emission tomography. Neurol Res 22: 457–464
29. Meier P, Zierler KL (1954) On the theory of the indicator-dilution method for measurement of blood flow and volume. J Appl Physiol 6:731–744
30. Piepmeier J, Baehring JM (2004) Surgical resection for patients with benign primary brain tumors and low grade gliomas. J Neurooncol 69:55–65
31. Beppu T, Inoue T, Nishimoto H, Ogasawara K, Ogawa A, Sasaki M (2007) Preoperative imaging of superficially located glioma resection using short inversion-time inversion recovery images in high-field magnetic resonance imaging. Clin Neurol Neurosurg 109:327–334
32. Cha S, Tihan T, Crawford F, Fischbein NJ, Chang S, Bollen A, Nelson SJ, Prados M, Berger MS, Dillon WP (2005) Differentiation of low-grade oligodendrogliomas from low-grade astrocytomas by using quantitative blood-volume measurements derived from dynamic susceptibility contrast-enhanced MR imaging. Am J Neuroradiol 26:266–273
33. Lev MH, Ozsunar Y, Henson JW, Rasheed AA, Barest GD, Harsh GR IV, Fitzek MM, Chiocca EA, Rabinov JD, Csavoy AN, Rosen BR, Hochberg FH, Schaefer PW, Gonzalez RG (2004) Glial tumor grading and outcome prediction using dynamic spin-echo MR susceptibility mapping compared with conventional contrast-enhanced MR: confounding effect of elevated rCBV of oligodendrogliomas. Am J Neuroradiol 25:214–221
34. Maia AC Jr, Malheiros SM, da Rocha AJ, da Silva CJ, Gabbai AA, Ferraz FA, Stavale JN (2005) MR cerebral blood volume maps correlated with vascular endothelial growth factor expression and tumor grade in nonenhancing gliomas. Am J Neuroradiol 26:777–783

MOLECULAR IMAGING AND BIOLOGY

Mol Imaging Biol (2013)
DOI: 10.1007/s11307-013-0670-7

World Molecular Imaging Society

RESEARCH ARTICLE

Standardized Uptake Value in High Uptake Area on Positron Emission Tomography with ^{18}F-FRP170 as a Hypoxic Cell Tracer Correlates with Intratumoral Oxygen Pressure in Glioblastoma

Takaaki Beppu,[1] Kazunori Terasaki,[2] Toshiaki Sasaki,[2] Shunrou Fujiwara,[1] Hideki Matsuura,[1] Kuniaki Ogasawara,[1] Koichiro Sera,[2] Noriyuki Yamada,[3] Noriyuki Uesugi,[3] Tamotsu Sugai,[3] Kohsuke Kudo,[4] Makoto Sasaki,[4] Shigeru Ehara,[5] Ren Iwata,[6] Yoshihiro Takai[7]

[1]*Department of Neurosurgery, Iwate Medical University, Uchimaru 19-1, Morioka 020-8505, Japan*
[2]*Cyclotron Research Center, Iwate Medical University, Morioka, Japan*
[3]*Department of Clinical Pathology, Iwate Medical University, Morioka, Japan*
[4]*Institute for Biomedical Sciences, Iwate Medical University, Morioka, Japan*
[5]*Department of Radiology, Iwate Medical University, Morioka, Japan*
[6]*Cyclotron and Radioisotope Center (CYRIC), Tohoku University, Sendai, Japan*
[7]*Department of Radiology and Radiation Oncology, Hirosaki University Graduate School of Medicine, Hirosaki, Japan*

Abstract

Purpose: The aim of this study was to clarify the reliability of positron emission tomography (PET) using a new hypoxic cell tracer, 1-(2-[^{18}F]fluoro-1-[hydroxymethyl]ethoxy)methyl-2-nitroimidazole (^{18}F-FRP170).

Procedures: Twelve patients with glioblastoma underwent ^{18}F-FRP170 PET before tumor resection. Mean standardized uptake value (SUV) and normalized SUV were calculated at regions within a tumor showing high (high-uptake area) and relatively low (low-uptake area) accumulations of ^{18}F-FRP170. In these areas, intratumoral oxygen pressure (tpO_2) was measured using microelectrodes during tumor resection.

Results: Mean tpO_2 was significantly lower in the high-uptake area than in the low-uptake area. A significant negative correlation was evident between normalized SUV and tpO_2 in the high-uptake area.

Conclusion: The present findings suggest that high accumulation on ^{18}F-FRP170 PET represents viable hypoxic tissues in glioblastoma.

Key words: F-FRP170, PET, Hypoxia, Glioblastoma, Oxygen pressure, HIF1-α

Abbreviation: Cu-ATSM, ^{64}Cu-diacetyl-bis(N4-methylthiosemicarbazone); ^{18}F-FRP170, 1-(2-[^{18}F]fluoro-1-[hydroxymethyl]ethoxy)methyl-2-nitroimidazole; ^{18}F-FAZA, 1-α-D-(5-deoxy-5-[^{18}F]-fluoroarabinofuranosyl)-2-nitroimidazole; ^{18}F-FMISO, [^{18}F]fluoromisonidazole; Gd-T1WI, Gadolinium-enhanced T1-weighted imaging; HIF, Hypoxic-inducible factor; MRI, Magnetic resonance imaging; ROI, Region of interest; T2WI, T2-weighted imaging; PET, Positron emission tomography; VEGF, Vascular endothelial growth factor

Correspondence to: Takaaki Beppu; *e-mail:* tbeppu@iwate-med.ac.jp

Published online: 20 July 2013

Introduction

Almost all malignant solid tumors include hypoxic cells due to both excessive consumption and insufficient supply of oxygen within the tumor. Intratumoral hypoxia induces various biological characteristics in tumors. For instance, hypoxia in tumor activates the hypoxia-responsive elements such as hypoxia-inducible factors (HIFs), leading to transcription of target genes including vascular endothelial growth factor (VEGF). VEGF induces angiogenesis, and is also closely related to the proliferation and invasion of tumor. Gene instability caused by hypoxia must affect the differentiation of tumor cells. Intratumoral hypoxic conditions are disadvantageous in term of the production of peroxide radicals, which induces DNA damage under irradiation. Cancer stem cells existing within hypoxic tumor tissue have also been considered to represent a likely cause of radioresistance [1–3]. In glioblastoma, hypoxic conditions play a key role in the development of tumor characteristics. Neuroimaging enabling minimally invasive, objective, and quantitative evaluation of hypoxic conditions in glioblastoma would offer many clinical benefits in terms of diagnosis, selection of treatment, and prediction of prognosis.

Positron emission tomography (PET) using hypoxic cell tracers offers an attractive method for detecting hypoxic cells because it is simple, low-invasive, repeatable, and not limited in applicability to superficial tumors [4]. So far, hypoxic cells in brain tumors have been detected using PET with hypoxic cell tracers such as [^{18}F]fluoromisonidazole (^{18}F-FMISO) [5–7], 1-α-D-(5-deoxy-5-5-[^{18}F]-fluoroarabinofuranosyl)-2-nitroimidazole (^{18}F-FAZA) [8], and ^{64}Cu-diacetyl-bis(N4-methylthiosemicarbazone) (Cu-ATSM) [9, 10]. A new hypoxic cell tracer, 1-(2-[^{18}F]fluoro-1-[hydroxymethyl]ethoxy)methyl-2-nitroimidazole (^{18}F-FRP170), has recently been identified [11, 12]. PET using ^{18}F-FRP170 (^{18}F-FRP170 PET) has already been performed for detecting hypoxic cells in malignant brain tumors, and the potential of this new tracer has been documented [13]. Several studies assessing intratumoral oxygen condition using electrodes or other methods have confirmed reliability of PET with various hypoxic cell tracers other than ^{18}F-FRP170 [14–17]. However, whether areas of high accumulation on ^{18}F-FRP170 PET really represent tissues including hypoxic cells, and to what degree areas of high accumulation represent regions under hypoxic conditions have remained unclear. The aim of this study was to confirm the reliability of ^{18}F-FRP170 PET for detecting hypoxic cells. We therefore compared standardized uptake value (SUV) measured on ^{18}F-FRP170 PET with intratumoral oxygen pressure (tpO_2) within glioblastoma measured using oxygen microelectrodes during tumor resection. Furthermore, we performed immunohistochemical detection HIF-1, a heterodimeric nuclear transcription factor playing a critical role in cellular response to low oxygen pressure [18], in tissues corresponding to the regions of interest (ROIs) on ^{18}F-FRP170 PET images.

Materials and Methods

Patients

All study protocols were approved by the Ethics Committee of Iwate Medical University, Morioka, Japan (No. H22-70). Patients recruited to this study were admitted to Iwate Medical University Hospital between April 2008 and December 2012. Entry criteria for the study were: patients ≥20 years old with non-treated glioblastoma localized in cerebral white matter other than the brain stem or cerebellum, performance of ^{18}F-FRP170 PET and measurement of absolute oxygen pressure within the tumor according to the study protocol, and voluntary provision of written informed consent to participate. Preoperative diagnosis was based on present history and findings from conventional magnetic resonance imaging (MRI) on admission, and final diagnosis of glioblastoma was made based on histological features after surgery. Twelve patients (ten men, two women, mean age, 63±13.7 years) were enrolled after excluding patients who did not meet the entry criteria (Table 1).

^{18}F-FRP170 PET

Within 7 days (mean, 4.3±2.4 days) before surgery for tumor resection, both conventional MRI including gadolinium-enhanced T1-weighted imaging (Gd-T1WI) and ^{18}F-FRP170 PET were performed. The ^{18}F-FRP170 was synthesized using on-column alkaline hydrolysis according to the methods described by Ishikawa et al. [12]. The final formulation for injection was formed in normal saline containing 2.5 %*v/v* ethanol using solid-phase extraction techniques. At 60 min after intravenous injection of approximately 370 MBq (mean, 5.9±1.8 MBq/kg) of ^{18}F-FRP170, PET was performed using a PET/computed tomography (CT) system (SET3000 GCT/M; Shimazu, Japan). On ^{18}F-FRP170 PET, ROIs of 10 mm in diameter were placed at areas of high accumulation (high-uptake area) and relatively low accumulation (low-uptake area) within the tumor bulk (Fig. 1a, b). These ROIs were placed at regions as close to the brain surface as possible to allow easy and safe insertion of microelectrodes for measuring oxygen pressure during surgery. A ROI was also placed in apparent normal cerebral white matter of the contralateral side. SUV for each ROI was automatically determined. Although both mean and maximal values of SUV in ROI were measured, we defined the mean value of SUV as "SUV" in this study. The normalized SUV, defined as SUV for each high- or low-uptake area divided by SUV for the apparent normal cerebral white matter of the contralateral hemisphere, was also calculated.

Immediately before surgery for each patient, we created a fusion image that combined a three-dimensional ^{18}F-FRP170 PET image with Gd-T1WI using a surgical navigation system (Stealth Station TRIA plus; Medtronics, Minneapolis, MN) in the operation room. On the fusion image, both high- and low-uptake areas were identified stereotactically for each patient (Fig. 2a–d).

Measurement of Intratumoral Oxygen Pressure During Surgery

Measurement of tpO_2 was performed during surgery for aggressive tumor resection. The tpO_2 level was measured using disposable

Table 1. Patient characteristics and measurement data

No.	Sex	Age (year)	Location	SUV			Normalized SUV		tpO_2 (mmHg)		PaO_2 (mmHg)	HIF-1α staining
				High uptake	Low uptake	ANWM	High uptake	Low uptake	High uptake	Low uptake		
1	M	76	Parietal lobe	0.99	0.54	0.54	1.83	1.00	23	44	157	−
2	M	81	Parietal lobe	2.22	1.39	1.04	2.13	1.34	16	45	128	−
3	M	59	Frontal lobe	1.46	1.16	0.87	1.69	1.33	28	56	176	−
4	F	61	Frontal lobe	1.10	0.87	0.74	1.49	1.18	32	54	145	−
5	M	75	Parietal lobe	1.83	1.11	0.83	2.20	1.34	16	33	143	−
6	F	54	Parietal lobe	1.43	0.82	0.62	2.31	1.32	30	54	134	−
7	M	64	Temporal lobe	1.62	1.00	0.72	2.25	1.39	15	27	158	+
8	M	54	Occipital lobe	1.50	1.01	0.76	1.97	1.33	17	35	120	+
9	M	67	Frontal lobe	1.84	1.46	1.13	1.63	1.29	25	36	132	+
10	M	76	Temporal lobe	1.90	0.92	0.77	2.47	1.19	15	26	124	+
11	M	58	Frontal lobe	1.37	1.25	0.90	1.52	1.39	24	34	137	+
12	M	31	Frontal lobe	1.66	1.11	0.87	1.91	1.28	20	37	148	+

ANWM apparent normal white matter, *tpO2* intratumoral oxygen pressure

Clark-type electrodes (UOE-04TS; Unique Medical, Tokyo, Japan) at the tip of a sensor (Teflon-coated tube; diameter, 0.4 mm; length, 10 mm). Immediately before surgery, electrodes were sterilized by immersion in a solution of 2.25 *w/v*% glutaraldehyde and buffer for 2 h, then washed with sterilized physiological saline solution. The electrode was then connected to a digital oxygen pressure monitor (POG-203; Unique Medical) to calibrate the value of oxygen pressure to 150 mmHg in a sterilized physiological saline solution prior to insertion into the tumor. After craniotomy, we stereotactically inserted a needle-shaped navigating marker of 2 mm in diameter into the center region of the high-uptake area where the ROI had been placed before surgery through the dura mater, while we observed the localization of the tip of the marker in the tumor on the monitor of the surgical navigation system (Fig. 2c, d). After removal of the navigation marker, we immediately inserted the electrode along the same trajectory through the dura mater, with the tip of the electrode placed within tumor tissue of the high-uptake area. A digital monitor was then used to measure tpO_2. We observed tpO_2 value gradually declined from 150 mmHg while rising and falling on the digital monitor, and defined the minimum value as the absolute tpO_2 value at the high-uptake area for each patient. After completely washing and calibrating the value of oxygen pressure to 150 mmHg in a sterilized physiological saline solution, the same procedure described above was performed to measure tpO_2 in the low-uptake area. During measurements of tpO_2, arterial oxygen pressure (PaO_2) was measured using arterial blood obtained from the radial artery. After measuring tpO_2 and removing the electrode, we inserted a needle for biopsy along a trajectory to obtain tumor tissues from the high- and low-uptake areas in six patients. In all cases, the tumor was successfully removed after completing the procedures described above.

HIF-1α Immunohistochemistry

Immunohistochemical staining of HIF-1α was performed on specimens obtained from tumor resection for six patients. From all specimens in both high- and low-uptake areas, paraffin-embedded tissue sections of 3-μm-thickness were collected onto 3-aminoprophyltriethoxylane-coated glass slides. The dewaxed preparations were given microwave pretreatment for 30 min in sodium citrate. The preparations were incubated for 60 min using rabbit anti-HIF-1α monoclonal antibody (clone, H1alpha67; Novus Biologicals, Littleton, CO) at 1:200 dilution. Preparations were incubated using peroxidase-based EnVision kits (Dako Japan, Tokyo, Japan) as the secondary antibody, then immersed in diaminobenzidine/H_2O_2 solution for colored visualization. Finally, preparations were counterstained with hematoxylin.

We observed the staining attitude of HIF-1α in tumor cells for all patients. We also evaluated the HIF-1α staining indices for each high- or low-uptake area for each patient, defined as the percentage of cells showing nuclear staining as determined by counting approximately 1,000 cells under light microscopy (×400 magnification).

Statistical Analyses

In all patients, differences in SUV, normalized SUV, and HIF-1α staining index were compared between high- and low-uptake areas using the Mann–Whitney *U* test. Differences in intratumoral pO_2 between high- and low-uptake areas were also compared in all patients using the Mann–Whitney *U* test. Correlations between PaO_2 and tpO_2 and between normalized SUV and tpO_2 for all patients were analyzed in each high- and low-uptake area using Pearson's correlation coefficient test.

Results

Scanning at 60 min after intravenous injection of tracer provided fine contrast images that enabled visual differentiation between high- and low-uptake areas in all patients. In eight patients with glioblastoma presenting a central necrotic region, ^{18}F-FRP170 was partially accumulated in the intermediate layer between the deep layer surrounding the central necrotic region and the outer layer within the peripheral region of tumor involved in lesion enhancement on Gd-T1WI (Fig. 1a, b). Fusion images combining Gd-T1WI and ^{18}F-FRP170 PET provided precise locations of both high- and low-uptake regions during surgery, and allowed us to successfully insert electrodes and obtain the

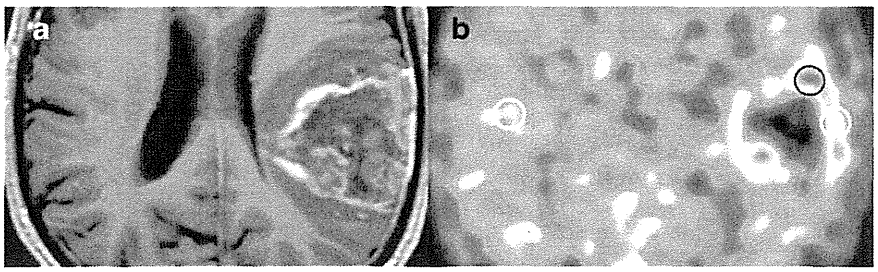

Fig. 1. Typical findings of ^{18}F-FRP170 PET in glioblastoma with a large area of central necrosis in Case 1. High-uptake areas are seen partially in the area between the outer peripheral region showing enhancement on Gd-T1WI and a deeper region adjacent to the central necrotic region. ROIs were placed on a high-uptake area (*black circle*) and a relatively low-uptake area (*white circle*) within the tumor bulk showing enhancement on Gd-T1W, and also on apparent normal white matter of the contralateral hemisphere (*white circle*). **a** Gd-T1WI, **b** ^{18}F-FRP170 PET.

sampling tissues (Fig. 2a–d). No patient presented with any complications due to ^{18}F-FRP170 PET.

Mean SUV for high-uptake areas, low-uptake areas, and contralateral normal white matter regions were 1.58±0.35, 1.05±0.25, and 0.82±0.16, respectively. Significant differences in mean SUV were found between high- and low-uptake areas (p=0.001), between high-uptake areas and normal white matter (p<0.001), and between low-uptake areas and normal white matter (p=0.01), although SUV values in the three groups overlapped (Fig. 3a). Mean normalized SUV for the high- and low-uptake areas were calculated as 1.95±0.33 and 1.28±0.11, respectively. Mean normalized SUV for the high-uptake area differed significantly (p<0.001) and clearly from that of the low-uptake area, with a cut-off level of around 1.4 (Fig. 3b). Mean tpO_2 was significantly lower in high-uptake areas (21.7±

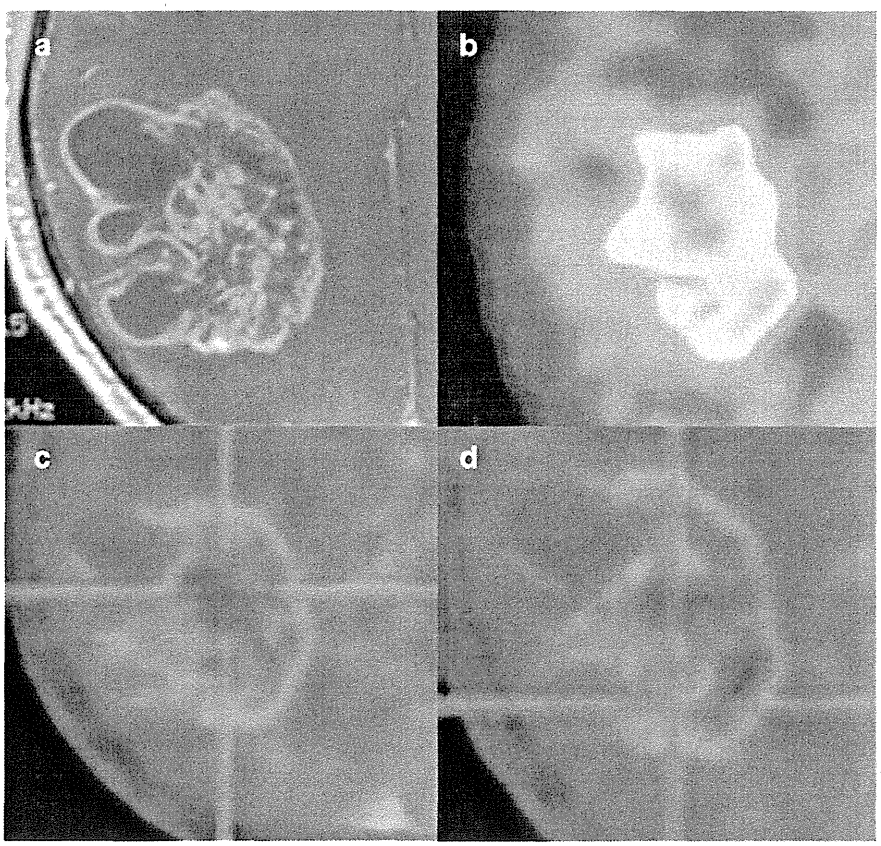

Fig. 2. High- and low-uptake areas were stereotactically localized on fusion images combining Gd-T1WI (**a**) and ^{18}F-FRP170 PET (**b**) for Case 5, to identify tumor tissues corresponding to ROIs. On fusion images, high- and low-uptake areas were depicted as bluish regions (**c**) and greenish regions (**d**), respectively.

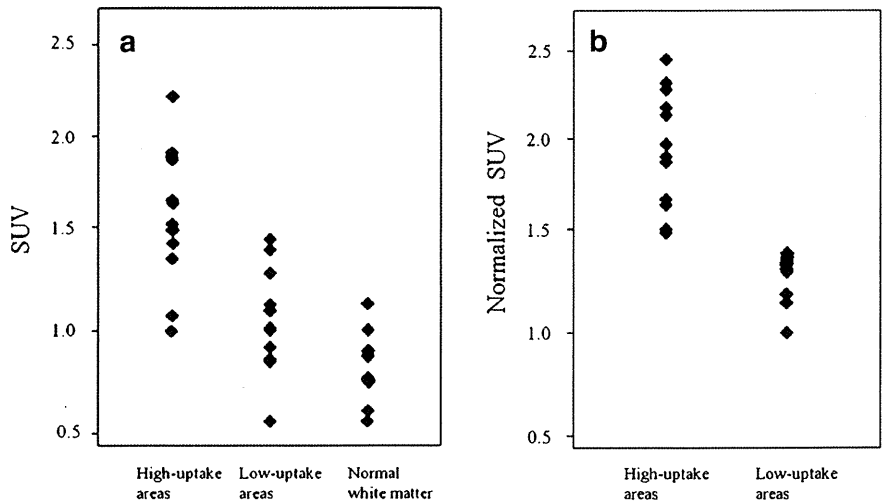

Fig. 3. **a** Differences in SUV among the high-uptake area, low-uptake area, and apparent normal white matter. **b** Difference in normalized SUV between high- and low-uptake areas.

6.2 mmHg) than in low-uptake areas (40.1±10.4 mmHg; $p<0.001$, Fig. 4). In terms of the relationship between normalized SUV and tpO_2 in all patients, a significant negative correlation was found in high-uptake areas ($r=-0.64$, $p=0.03$), whereas no significant correlation was identified in low-uptake areas (Fig. 5a, b). No significant correlations between PaO_2 and tpO_2 were found in either high- or low-uptake areas (not shown).

On specimens obtained from high-uptake areas, HIF-1α was clearly detectable in nuclei in all six patients, with three patients also showing HIF-1α staining in cytoplasm. On the other hand,

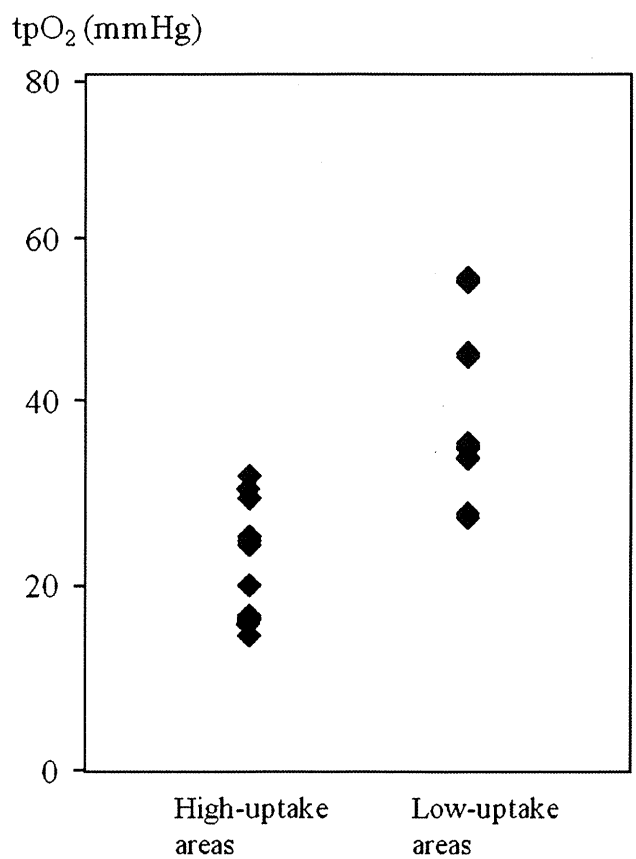

Fig. 4. Difference in tpO_2 between high- and low-uptake areas.

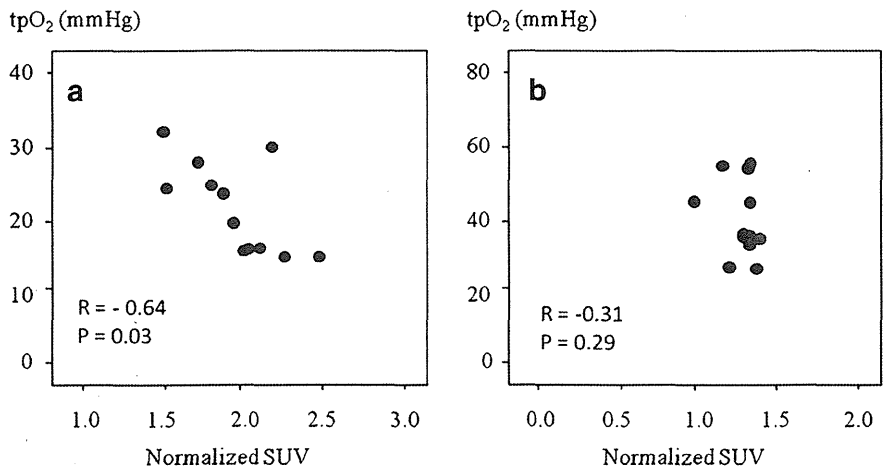

Fig. 5. Correlations between normalized SUV and tpO_2 in high-uptake areas (**a**) and low-uptake areas (**b**).

specimens from low-uptake areas showed three different patterns, with HIF-1α staining only cytoplasm in three patients, and both nuclei and cytoplasm in two patients. In the remaining patient, few barely surviving cells with HIF-1α staining were seen within a wide area of necrotic tissue (Fig. 6a–d). HIF-1α staining indices ranged from 35.2 to 63.5 % in high-uptake areas, and from 8.9 to 35.9 % in low-uptake areas. Mean HIF-1α staining index was significantly higher in high-uptake areas (mean, 53.0±10.2 %) than in low-uptake areas (mean, 18.9± 9.5 %). Notably, HIF-1α staining index was markedly low (8.9 %) in necrotic tissue obtained from a low-uptake area in one patient.

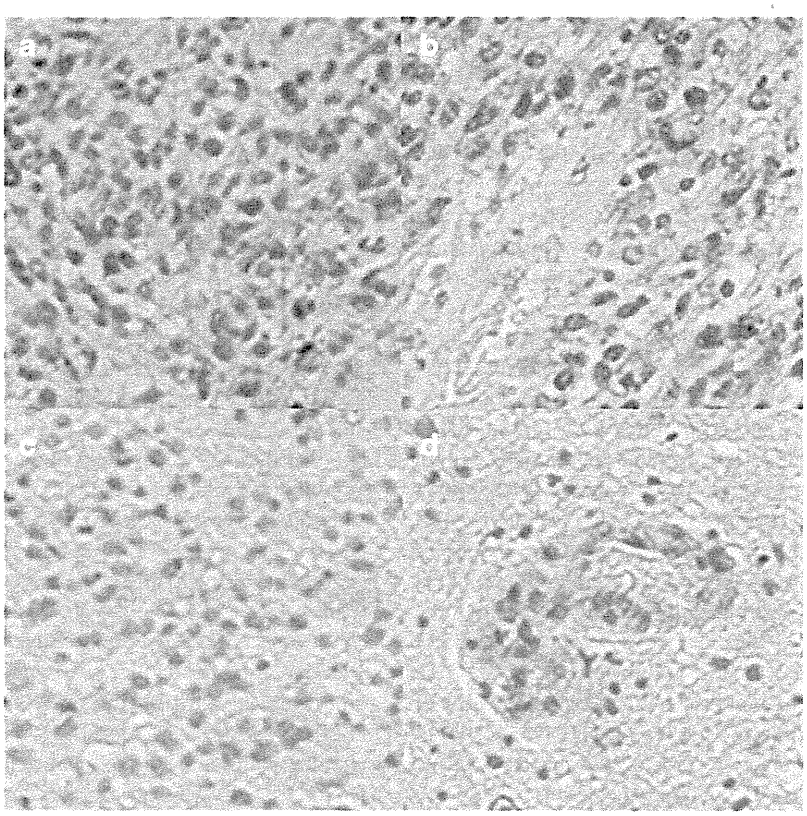

Fig. 6. Findings for HIF-1α immunostaining of tissues from high-uptake areas (**a**, **b**) and low-uptake areas (**c**, **d**). **a** HIF-1α was strongly detected in nuclei in all patients. **b** HIF-1α was stained in both cytoplasms and nuclei in three patients. **c** HIF-1α was stained only in cytoplasm in three patients. **d** A few HIF-1α-stained cells were seen within a wide necrotic tissue in one patient.

Discussion

The present study showed that mean values of both SUV and normalized SUV were significantly higher in high-uptake areas than in low-uptake areas. In particular, normalized SUV values in high-uptake areas were absolutely higher than those in low-uptake areas. In this study, approximately 370 MBq of ^{18}F-FRP170 was administered intravenously for all patients, according to a report by Shibahara et al. [13]. Absolute SUV might thus have been subtly influenced by the delivered volume of tracer into the tumor as determined by individual parameters, such as body size, cardiac output volume, and blood pressure. As normalization of absolute SUV can eliminate differences in these factors, we emphasize the importance of estimation using normalized SUV. In the present study, tpO_2 did not correlate with PaO_2 at all. Two previous reports examining both tpO_2 in brain tumors and PaO_2 could not find any relationship between these measured values, although correlations were not estimated statistically [19, 20]. Our results support those previous reports and indicate that tpO_2 was not influenced by PaO_2 during surgery. Values of tpO_2 were significantly lower in high-uptake areas (21.7± 6.2 mmHg) than in low-uptake areas (40.1±10.4 mmHg). Furthermore, a significant correlation was found between normalized SUV and tpO_2 in high-uptake areas. These results indicate that high-uptake areas where ^{18}F-FRP170 accumulates show relatively more hypoxic conditions than low-uptake areas, suggesting the reliability of findings from ^{18}F-FRP170 PET.

Selective accumulation of ^{8}F-FRP170 in hypoxic cells has been considered to proceed as follows. First, the nitroimidazole moiety in ^{18}F-FRP170 is responsible for the initial accumulation in hypoxic cells. After passive diffusion inside the cells, enzymatic nitroreduction by nitroreductase results in nitroimidazole changing to radical anions. Under normoxic conditions, these radical anions are reoxidized and diffuse out of the cells, whereas products comprising radical anions covalently bound to intracellular macromolecules are trapped within cells under hypoxic conditions [13, 21–23]. As a result, ^{18}F-FRP170 can accumulate only within viable and active hypoxic cells, but cannot accumulate within normoxic cells or even hypoxic cells with low metabolism such as apoptotic or necrotic cells. A previous report assessing accumulation of ^{18}F-FRP170 in a rat model of ischemic myocardium using autoradiography documented that ^{18}F-FRP170 was observed only within viable hypoxic myocardiac cells [11]. As absolute SUV must correlate with the concentration of PET tracer within the tissue, SUV on ^{18}F-FRP170 PET should increase with a higher density of viable hypoxic cells within the tissues of the ROI. We think that such high-uptake areas represent glioblastoma tissue comprising a high density of viable hypoxic cells. In contrast, tissues of low-uptake areas might represent low densities of viable hypoxic cells. In other words, a majority of cells in low-uptake areas could not accumulate ^{18}F-FRP170 because of the presence of either viable cells containing relatively higher tpO_2 than high-uptake area or low metabolic-hypoxic cells degenerating in apoptosis or necrosis. The oxygen environment may thus differ substantially among different regions in low-uptake areas, despite the similar content of viable hypoxic cells. Indeed, tpO_2 levels showed a wide range in low-uptake areas, with a large standard deviation (Fig. 4). This might be one reason for the lack of significant correlation between tpO_2 levels and normalized SUV in low-uptake areas. As intratumoral hypoxia is generally considered to result from insufficient oxygen supply paralleling the distance from normal vessels surrounding the tumor, intratumoral oxygen pressure should be higher in more peripheral regions of glioblastoma that are also supplied with blood from normal vessels surrounding the tumor bulk [24, 25]. On PET in the present study, interestingly, high-uptake areas were observed partially within the intermediate layer of enhancing lesions on Gd-T1WI, and low-uptake areas were seen not only in the peripheral layer external to the intermediate layer containing high-uptake areas but also in the inner core layer adjacent to the central necrosis deep to the intermediate layer (Fig. 1b). We assumed that low-uptake areas in both peripheral and inner core layers might contain little ^{18}F-FRP170-accumulating hypoxic cells, but the peripheral layers included many viable cells at relatively high oxygen pressure, while the inner core comprises low metabolic-hypoxic cells undergoing degenerative apoptosis or necrosis. Remaining low-uptake areas in the intermediate layer probably represent mixture of the two histological types described above. Pistollato et al. [26] evaluated biological characteristics in tissues isolated from three concentric layers (core, intermediate, and peripheral layers) in glioblastoma. The core and intermediate layers showed expression of HIF-1α as a hypoxic cell marker, whereas the peripheral layer did not express HIF-1α, but showed expressions of glial fibrillary acidic protein and β-III-tubulin as mature neural cell markers. In addition, core and intermediate layers contained more glioblastoma stem cells, which are well known to be frequently seen in hypoxic niches. These results suggest that inner core and peripheral layers depicted as low-uptake areas on ^{18}F-FRP170 PET in the present study are likely to exhibit hypoxic and relatively normoxic conditions, respectively.

Hypoxic condition rapidly induces overexpression of HIF-1α for transcripting target genes such as vascular endothelial growth factor to induce angiogenesis, as countermeasures against hypoxic conditions. Under normoxic conditions, prolyl hydroxylation is induced in HIF-1α, allowing binding to the von-Hipple-Lindau protein, which mediates ubiquitination of HIF-1α and subsequent proteasomal degeneration in the cytoplasm. However, under hypoxic conditions, the oxygen requiring prolyl hydroxylase remains inactive, resulting in accumulation of the constitutively expressed HIF-1α protein in cytoplasm. This subunit is phosphorylated and translocated to the nucleus, where it dimerizes with the HIF-1β subunit, binding to the hypoxia-

response elements upstream of HIF-1-regulated target genes [27]. Therefore, increasingly activated-HIF-1α induced by hypoxia accumulates in the nucleus. In this study, all specimens obtained from high-uptake areas clearly showed nuclear staining for HIF-1α, whereas this finding was seen in low-uptake areas in only two patients. Furthermore, mean HIF-1α staining index determined by the percentage of cells showing nuclear staining was significantly higher in high-uptake areas than in low-uptake areas. Necrotic tissue obtained from a low-uptake area of one patient showed an extremely low HIF-1α staining index. These findings might support the concept that high-uptake areas represent more hypoxic regions with a high density of viable and active hypoxic cells. Tissues of low-uptake areas were not obtained from deeper than high-uptake areas but rather from the same depth or more externally during surgery in all six patients. As a result, HIF-1α was also detected in the low-uptake areas of all patients, but showed a greater variety of features than high-uptake areas. These findings support the possibility that low-uptake areas comprised either numerous viable cells under conditions of relatively higher oxygen pressure or low metabolic hypoxic cells under degenerative apoptosis or necrosis.

In the present study, PET at 60 min after intravenous injection of ^{18}F-FRP170 could provide visually fine-contrast PET images. Shidehara et al. [13] reported fine-contrast color images provided by imaging at 120 min after injection of ^{18}F-FRP170 in patients with malignant brain tumor. Kaneta et al. [21] reported that imaging results at 120 min after injection of ^{18}F-FRP170 for patients with lung cancer contributed only a slightly higher tumor/blood ratio when compared with that at 60 min, and concluded that imaging at 60 min after administration was clinically sufficient for assessing hypoxic cells in tumors. The present study supported these recommendations by Kaneta et al. In an experimental study using mice bearing cultured cancer cells, ^{18}F-FAZA displayed significant higher tumor-to-background ratios compared with ^{18}F-FMISO and another azomycin-based nucleoside, iodoazomycin arabinoside, labeled with ^{124}I (^{124}I-IAZA), when scanning for all tracer was fixed in 3 h post-injection [28]. Clinically, PET imaging with ^{18}F-FMISO and ^{18}F-FAZA has usually been scanned at 120–140 [5–7] and 120–210 min [8] after administration, respectively. Although no previous reports have directly compared ^{18}F-FRP170 PET and ^{18}F-FMISO PET images, ^{18}F-FRP170 PET has been considered superior in terms of fine contrast and rapid clearance from blood [21]. The short duration for imaging could represent an additional advantage to ^{18}F-FRP170 PET.

Some limitations regarding the interpretation of study results must be considered for this study. First, the sample size in this study was small. Additional studies of a larger number of patients with glioblastoma are needed. Second, use of smaller ROIs might provide more rigorous results in comparisons among SUV, tpO_2, and histological features. However, in this study, we placed relatively huge ROIs of 10 mm in diameter to avoid misplacement of microelectrodes within the ROI and sampling error of tumor tissues corresponding to the ROI. These issues could represent factors contributing to make maximum SUV within the ROI unsuitable for use in this study. In short, errors involving differences between pinpoint regions for insertion of electrode and maximum SUV could easily anticipated. Third, direct tpO_2 measurements using microelectrodes available differ in sensitivity, accuracy, ability to measure oxygen availability among types of probe used, and impossibility in differentiation between hypoxic and necrotic tissues, although this technique is commonly considered a gold standard [4]. Other techniques indirectly measuring oxygen through reduced drug levels, hemoglobin saturation, or perfusion have been proposed. However, indirect measurements, although valuable, require a set of assumptions to relate the measurement to tpO_2 or oxygen concentration [4]. Fourth, measurement of tpO_2 using electrodes in this study did not strictly represent intracellular oxygen pressure, but rather the oxygen pressure of tissue containing hypoxic cells. However, tpO_2 as measured in this study would correlate with intracellular oxygen pressure, as intracellular oxygen pressure is regulated by extracellular conditions. Fifth, measured tpO_2 values in this study were relatively higher (21.7±6.2 mmHg in high-uptake areas and 40.1±10.4 mmHg in low-uptake areas) than in previous reports of direct measurement using Eppendorf oxygen electrodes in malignant brain tumors, where mean tpO_2 has been reported as approximately ≤20 mmHg [20, 24, 29]. In particular, mean value in low-uptake areas was significantly higher. However, mean tpO_2 in low-uptake areas was lower that of brain tissue around the tumor (59.8±6.5 mmHg) in a previous report [20]. In previous reports regarding oxygen pressure at high-uptake areas on ^{18}F-FMISO PET in animal tumor models, measurements using Eppendorf electrodes showed a high frequency of tpO_2 ≤10 mmHg [15, 30, 31]. Although the reasons for this contradiction are not entirely clear, we consider these results may have arisen from differences in the electrodes used, or from the inflow of a small amount of air into the trajectory when electrodes were inserted immediately after removal of the navigation marker with a larger diameter than the electrode. However, as this issue applied to measurements of tpO_2 for all patients in this study, the findings of higher tpO_2 in high-uptake areas compared to low-uptake areas appear valid.

Conclusions

Findings of a significant correlation between normalized SUV and tpO_2, and strong nuclear immunostaining for HIF-1α in areas of high ^{18}F-FRP170 accumulation, suggest that high-uptake areas on ^{18}F-FRP170 PET represent high densities of viable hypoxic cells, at least in glioblastoma. However, interpretation of low-uptake areas is more complicated, given the likelihood that these lesions comprise

various oxygen environments containing low densities of viable hypoxic cells.

Acknowledgments. This study was supported in part by Grant-in-Aid for Strategic Medical Science Research Center for Advanced Medical Science Research from the Ministry of Science, Education, Sports and Culture, Japan.

Conflict of Interest. The authors declare that they have no conflicts of interest.

References

1. Jensen RL (2009) Brain tumor hypoxia: tumorigenesis, angiogenesis, imaging, pseudoprogression, and as a therapeutic target. J Neurooncol 92:317–335
2. Jensen RL (2006) Hypoxia in the tumorigenesis of gliomas and as a potential target for therapeutic measures. Neurosurg Focus 20:E24
3. Rich JN (2007) Cancer stem cells in radiation resistance. Cancer Res 67:8980–8984
4. Mendichovszky I, Jackson A (2011) Imaging hypoxia in gliomas. Br J Radiol 84(2):S145–S158
5. Eschmann SM, Paulsen F, Reimold M et al (2005) Prognostic impact of hypoxia imaging with 18F-misonidazole PET in non-small cell lung cancer and head and neck cancer before radiotherapy. J Nucl Med 46:253–260
6. Kawai N, Maeda Y, Kudomi N et al (2011) Correlation of biological aggressiveness assessed by 11C-methionine PET and hypoxic burden assessed by 18F-fluoromisonidazole PET in newly diagnosed glioblastoma. Eur J Nucl Med Mol Imaging 38:441–450
7. Swanson KR, Chakraborty G, Wang CH et al (2009) Complementary but distinct roles for MRI and 18F-fluoromisonidazole PET in the assessment of human glioblastomas. J Nucl Med 50:36–44
8. Postema EJ, McEwan AJ, Riauka TA et al (2009) Initial results of hypoxia imaging using 1-alpha-D: -(5-deoxy-5-[^{18}F]-fluoroarabinofuranosyl)-2-nitroimidazole (^{18}F-FAZA). Eur J Nucl Med Mol Imaging 36:1565–1573
9. Sheehan JP, Popp B, Monteith S et al (2011) Trans sodium crocetinate: functional neuroimaging studies in a hypoxic brain tumor. J Neurosurg 115:749–753
10. Tateishi K, Tateishi U, Sato M et al (2013) Application of ^{62}Cu-diacetyl-bis (N4-methylthiosemicarbazone) PET imaging to predict highly malignant tumor grades and hypoxia-inducible factor-1alpha expression in patients with glioma. AJNR Am J Neuroradiol 34:92–99
11. Kaneta T, Takai Y, Kagaya Y et al (2002) Imaging of ischemic but viable myocardium using a new 18F-labeled 2-nitroimidazole analog, 18F–FRP170. J Nucl Med 43:109–116
12. Ishikawa Y, Iwata R, Furumoto S, Takai Y (2005) Automated preparation of hypoxic cell marker [^{18}F]FRP-170 by on-column hydrolysis. Appl Radiat Isot 62:705–710
13. Shibahara I, Kumabe T, Kanamori M et al (2010) Imaging of hypoxic lesions in patients with gliomas by using positron emission tomography with 1-(2-[^{18}F] fluoro-1-[hydroxymethyl]ethoxy)methyl-2-nitroimidazole, a new 18F-labeled 2-nitroimidazole analog. J Neurosurg 113:358–368
14. Matsumoto K, Szajek L, Krishna MC et al (2007) The influence of tumor oxygenation on hypoxia imaging in murine squamous cell carcinoma using [^{64}Cu]Cu-ATSM or [^{18}F]Fluoromisonidazole positron emission tomography. Int J Oncol 30:873–881
15. Sorensen M, Horsman MR, Cumming P et al (2005) Effect of intratumoral heterogeneity in oxygenation status on FMISO PET, autoradiography, and electrode Po2 measurements in murine tumors. Int J Radiat Oncol Biol Phys 62:854–861
16. Mahy P, De Bast M, Gallez B et al (2003) In vivo colocalization of 2-nitroimidazole EF5 fluorescence intensity and electron paramagnetic resonance oximetry in mouse tumors. Radiother Oncol 67:53–61
17. Tran LB, Bol A, Labar D et al (2012) Hypoxia imaging with the nitroimidazole ^{18}F-FAZA PET tracer: a comparison with OxyLite, EPR oximetry and 19F-MRI relaxometry. Radiother Oncol 105:29–35
18. Wang GL, Semenza GL (1995) Purification and characterization of hypoxia-inducible factor 1. J Biol Chem 270:1230–1237
19. Collingridge DR, Piepmeier JM, Rockwell S, Knisely JP (1999) Polarographic measurements of oxygen tension in human glioma and surrounding peritumoural brain tissue. Radiother Oncol 53:127–131
20. Kayama T, Yoshimoto T, Fujimoto S, Sakurai Y (1991) Intratumoral oxygen pressure in malignant brain tumor. J Neurosurg 74:55–59
21. Kaneta T, Takai Y, Iwata R et al (2007) Initial evaluation of dynamic human imaging using ^{18}F-FRP170 as a new PET tracer for imaging hypoxia. Ann Nucl Med 21:101–107
22. Chapman JD (1979) Hypoxic sensitizers—implications for radiation therapy. N Engl J Med 301:1429–1432
23. Krohn KA, Link JM, Mason RP (2008) Molecular imaging of hypoxia. J Nucl Med 49(Suppl 2):129S–148S
24. Beppu T, Kamada K, Yoshida Y et al (2002) Change of oxygen pressure in glioblastoma tissue under various conditions. J Neurooncol 58:47–52
25. Brown JM (1979) Evidence for acutely hypoxic cells in mouse tumours, and a possible mechanism of reoxygenation. Br J Radiol 52:650–656
26. Pistollato F, Abbadi S, Rampazzo E et al (2010) Intratumoral hypoxic gradient drives stem cells distribution and MGMT expression in glioblastoma. Stem Cells 28:851–862
27. Fischer I, Gagner JP, Law M, Newcomb EW, Zagzag D (2005) Angiogenesis in gliomas: biology and molecular pathophysiology. Brain Pathol 15:297–310
28. Reischl G, Dorow DS, Cullinane C et al (2007) Imaging of tumor hypoxia with [^{124}I]IAZA in comparison with [^{18}F]FMISO and [^{18}F]FAZA-first small animal PET results. J Pharm Pharm Sci 10:203–211
29. Rampling R, Cruickshank G, Lewis AD et al (1994) Direct measurement of pO2 distribution and bioreductive enzymes in human malignant brain tumors. Int J Radiat Oncol Biol Phys 29:427–431
30. Piert M, Machulla H, Becker G et al (1999) Introducing fluorine-18 fluoromisonidazole positron emission tomography for the localisation and quantification of pig liver hypoxia. Eur J Nucl Med 26:95–109
31. Bartlett RM, Beattie BJ, Naryanan M et al (2012) Image-guided PO2 probe measurements correlated with parametric images derived from ^{18}F-fluoromisonidazole small-animal PET data in rats. J Nucl Med 53:1608–1615

JJCO Japanese Journal of Clinical Oncology

Original Articles

Jpn J Clin Oncol 2012;42(10)887–895
doi:10.1093/jjco/hys121
Advance Access Publication 27 July 2012

Phase II Study of Single-agent Bevacizumab in Japanese Patients with Recurrent Malignant Glioma†

Motoo Nagane[1,*], Ryo Nishikawa[2], Yoshitaka Narita[3], Hiroyuki Kobayashi[4], Shingo Takano[5], Nobusada Shinoura[6], Tomokazu Aoki[7], Kazuhiko Sugiyama[8], Junichi Kuratsu[9], Yoshihiro Muragaki[10], Yutaka Sawamura[11] and Masao Matsutani[2]

[1]Department of Neurosurgery, Kyorin University Faculty of Medicine, Tokyo, [2]Department of Neuro-Oncology/Neurosurgery, International Medical Center, Saitama Medical University, Saitama, [3]Department of Neurosurgery and Neuro-Oncology, National Cancer Center Hospital, Tokyo, [4]Department of Neurosurgery, Graduate School of Medicine, Hokkaido University, Hokkaido, [5]Department of Neurosurgery, Graduate School of Human Science, University of Tsukuba, Ibaraki, [6]Department of Neurosurgery, Komagome Metropolitan Hospital, Tokyo, [7]Department of Neurosurgery, Kitano Hospital, Osaka, [8]Depatment of Neurosurgery, Hiroshima University School of Medicine, Hiroshima, [9]Department of Neurosurgery, Kumamoto University Faculty of Life Sciences, Kumamoto, [10]Faculty of Advanced Techno-Surgery Graduate School of Medicine, Tokyo Women's Medical University, Tokyo and [11]Sawamura Neurosurgery Clinic, Hokkaido, Japan

*For reprints and all correspondence: Motoo Nagane, Department of Neurosurgery, Kyorin University Faculty of Medicine, 6-20-2 Shinkawa, Mitaka, Tokyo 181-8611, Japan. E-mail: nagane-nsu@umin.ac.jp

†These data were previously presented at the 2011 European Multidisciplinary Cancer Congress, jointly organized by the European CanCer Organisation (ECCO) and European Society for Medical Oncology (ESMO), Stockholm, Sweden, 23–27 September 2011 and the 2011 Society for Neuro-Oncology, CA, USA, 17–20 November 2011.

Received April 18, 2012; accepted July 1, 2012

Objective: This single-arm, open-label, Phase II study evaluated the efficacy and safety of single-agent bevacizumab, a monoclonal antibody against vascular endothelial growth factor, in Japanese patients with recurrent malignant glioma.

Methods: Patients with histologically confirmed, measurable glioblastoma or World Health Organization Grade III glioma, previously treated with temozolomide plus radiotherapy, received 10 mg/kg bevacizumab intravenous infusion every 2 weeks. The primary endpoint was 6-month progression-free survival in the patients with recurrent glioblastoma.

Results: Of the 31 patients enrolled, 29 (93.5%) had glioblastoma and 2 (6.5%) had Grade III glioma. Eleven (35.5%) patients were receiving corticosteroids at baseline; 17 (54.8%) and 14 (45.2%) patients had experienced one or two relapses, respectively. The 6-month progression-free survival rate in the 29 patients with recurrent glioblastoma was 33.9% (90% confidence interval, 19.2–48.5) and the median progression-free survival was 3.3 months. The 1-year survival rate was 34.5% with a median overall survival of 10.5 months. There were eight responders (all partial responses) giving an objective response rate of 27.6%. The disease control rate was 79.3%. Eight of the 11 patients taking corticosteroids at baseline reduced their dose or discontinued corticosteroids during the study. Bevacizumab was well-tolerated and Grade ≥3 adverse events of special interest to bevacizumab were as follows: hypertension [3 (9.7%) patients], congestive heart failure [1 (3.2%) patient] and venous thromboembolism [1 (3.2%) patient]. One asymptomatic Grade 1 cerebral hemorrhage was observed, which resolved without treatment.

Conclusion: Single-agent bevacizumab provides clinical benefit for Japanese patients with recurrent glioblastoma.

Key words: bevacizumab – glioblastoma – Asian continental ancestry group – Phase II – glioma

INTRODUCTION

Glioblastoma (GBM) is the most aggressive form of primary malignant brain tumor and the prognosis for patients with GBM is poor (1,2); the majority will relapse following initial treatment and <10% are alive at 5 years (3). The standard treatment for patients with newly diagnosed GBM is surgical resection followed by temozolomide (TMZ) and radiotherapy (RT), and then adjuvant TMZ alone (Stupp regimen) (4). Treatment options for patients with recurrent GBM, however, are limited and include repeat resection, RT and systemic chemotherapy, such as TMZ, nitrosoureas, platinum-based regimens (carboplatin, cisplatin), cyclophosphamide, irinotecan and etoposide, and appropriate treatment will depend on the patient and tumor characteristics (5). Currently there is no standard therapy for recurrent GBM and the estimated 6-month progression-free survival (PFS) rate for patients with recurrent disease is 9–28% (6–11) with a 1-year survival rate of 14–32% (6–8,10,11). Therefore, new treatment strategies for recurrent GBM are needed.

An alternative therapeutic approach is the inhibition of angiogenesis through the vascular endothelial growth factor (VEGF), a key regulator of angiogenesis. High levels of VEGF are expressed in GBM cells (12,13), and hypoxia and acidosis, conditions commonly seen in solid tumors, upregulate VEGF expression in glioma cells *in vivo* (14). In a mouse model, monoclonal antibodies to VEGF have been shown to inhibit the growth of the C6 glioma (15). Bevacizumab (Avastin®) is a monoclonal antibody that inhibits VEGF and is currently approved for a range of metastatic cancers (colorectal, non-small-cell lung, breast, ovarian cancer and renal cancers) (16–19) as well as for use in adults with recurrent GBM in many countries including the USA (20,21). Early Phase II studies in patients with recurrent GBM showed the efficacy of bevacizumab in combination with irinotecan (22,23). Subsequently, two Phase II studies (24–26) showed the efficacy of single-agent bevacizumab with regard to response rates and 6-month PFS in patients with recurrent GBM who had previously received RT and TMZ. These two studies formed the basis of bevacizumab's approval by the Food and Drug Administration (FDA) in 2009. Moreover, other studies have shown the efficacy of bevacizumab in recurrent GBM whether given as a single agent (27) or combined with irinotecan (28,29) and other chemotherapies, such as etoposide, carboplatin and fotemustine (30–33). Given the current evidence for bevacizumab in recurrent GBM in Western patient populations, we investigated the efficacy and safety of single-agent bevacizumab in a Phase II, single-arm, open-label study (JO22506) in Japanese patients with recurrent malignant glioma.

PATIENTS AND METHODS

The trial was carried out in accordance with the principles of Good Clinical Practice and the Declaration of Helsinki; all patients provided written informed consent prior to any study-related procedure. The protocol was approved by the institutional review boards of all participating centers. The study was registered with the Japan Pharmaceutical Information Center-Clinical Trials Information (JapicCTI), trial number: JapicCTI-090841.

Eligibility

Eligible patients were aged ≥20 years with histologically confirmed GBM or World Health Organization (WHO) Grade III glioma, the latter being reconfirmed at the time of surgery for recurrent glioma. Patients had magnetic resonance imaging (MRI)-confirmed disease recurrence or progression with measurable lesions within 2 weeks prior to the first study treatment and no evidence of acute or subacute cerebral hemorrhage and had received prior TMZ and RT for malignant glioma. Other key inclusion criteria were a Karnofsky performance status (KPS) ≥70%, a life expectancy of ≥3 months and adequate hematologic, renal and hepatic function (i.e. absolute neutrophil count ≥1500/mm^3, platelet count ≥100 000/mm^3, hemoglobin ≥10 g/dl, bilirubin ≤ 1.5 × the upper limit of normal (ULN), aspartate aminotransferase and alanine aminotransferase ≤ 2.5 × ULN, serum creatinine ≤ 1.25 × ULN). The following minimum intervals of time must have elapsed between the termination of therapies and the start of bevacizumab treatment: RT 8 weeks; surgical therapy and incisional biopsy 4 weeks; endocrine therapy and immunotherapy 3 weeks; post-traumatic intervention (except for patients with non-healing wounds) 2 weeks; transfusion and the use of hematopoietic growth factors 2 weeks; aspiration cytology and needle biopsy 1 week; nitrosoureas 6 weeks, procarbazine 3 weeks, vincristine 2 weeks and other chemotherapies 4 weeks and other investigational new drugs and unapproved drugs 4 weeks. Patients were excluded if they had: prior treatment with bevacizumab; a history of treatment with carmustine wafers, stereotactic radiotherapy, proton therapy or neutron capture therapy; ≥3 prior regimens for malignant glioma and inadequately controlled hypertension, heart disease, symptomatic cerebrovascular disorder, gastrointestinal (GI) perforation, fistula or abdominal abscess within 6 months prior to enrollment.

Study Design

This single-arm, open-label, Phase II study was conducted at 10 sites in Japan. One cycle of treatment was defined as one